



Science Arts & Métiers (SAM)

is an open access repository that collects the work of Arts et Métiers Institute of Technology researchers and makes it freely available over the web where possible.

This is an author-deposited version published in: <https://sam.ensam.eu>
Handle ID: <http://hdl.handle.net/10985/15319>

To cite this version :

Paola CINNELLA, Xavier GLOERFELT - Investigation of the flow dynamics in a channel constricted by periodic hills - In: 45th AIAA Fluid Dynamics Conference, Etats-Unis, 2015 - 45th AIAA Fluid Dynamics Conference - 2015

Any correspondence concerning this service should be sent to the repository

Administrator : scienceouverte@ensam.eu



Investigation of the flow dynamics in a channel constricted by periodic hills

Xavier Gloerfelt^{1*} & Paola Cinnella^{1,2†}

¹ *Arts et Métiers ParisTech, DynFluid Laboratory, 75013 Paris, France*

² *Università del Salento, via per Monteroni, 73100, Lecce, Italy*

I. Introduction

To assess the reliability of numerical flow solver in complex engineering applications, there is a need for well-controlled benchmark configuration. A particularly challenging problem is the prediction of separation of turbulent flows from curved surface and subsequent reattachment. A benchmark case should have a sufficiently reduced complexity to be amenable to well-resolved simulation with current supercomputer capabilities. Such a test-case can help to validate and improve the turbulence closures either for Reynolds averaged Navier-Stokes (RANS) or Large Eddy Simulations (LES) equations. In the last ten years, the configuration of the flow in a channel constricted by periodic protusions has become an increasingly popular case to assess the performances of LES or RANS/LES solvers. The configuration which has emerged from trial and error consists in a plane channel of height L_y with two-dimensional curved constrictions, whose height h satisfies $L_y = 3.036h$. A periodicity is imposed in the streamwise direction x with a sufficiently large distance $L_x = 9h$ between two consecutive hills in order to allow a partial recovery of the flow after its reattachment and an acceleration on the windward wall of the next hill. The third direction z is assumed homogeneous, meaning that the span is very large and the flow can be considered as 2-D in the mean. The x - and z - periodicities are favourable insofar as the specification of a turbulent inlet condition is circumvented and the averaging along the span can be used to improve the statistical convergence, respectively. A Reynolds number is built from the hill height h , the bulk velocity at the top of the hill U_b and the kinematic viscosity of the fluid ν . Moderate values of this non-dimensional parameter are selected to achieve a fully turbulent state while maintaining the number of grid points for a well-resolved LES at tolerable cost. Most of the simulations for assessing LES or RANS/LES solvers have considered a value $Re=10\,595$, originally used by Mellen *et al.*¹ The incompressible regime is considered. A large variety of numerical methods, meshing strategies, subgrid-scale (SGS) models, wall modeling assumptions (through either RANS equations or wall functions) have been investigated in the past.^{2–12} Well-resolved LES have been published to serve as reference for the validation purposes.^{5,9} Furthermore, proper experiments have been designed to reproduce this flow configuration using 10 hills in a water tunnel to achieve periodicity in the streamwise direction and a very large extent in the spanwise direction. The setup and the measurement results are documented in Breuer *et al.*⁹ Data for the hill geometry, reference LES and measurements are made available as an ERCOFTAC database.¹³

Convincing comparisons between different codes and between experiments and simulations have given confidence that this benchmark is well-posed. Its success in the CFD community is visible through the choice as this benchmark case in several collaborative project funded by the European Union, *i.e.* DESIDER¹⁴ to investigate the reliability of several RANS/LES strategies or IDIHOM¹⁵ about the efficiency of high-order codes in industrial-like configurations. The flow was also a test case at 2 ERCOFTAC/IAHR/COST workshops and in the European ATAAC project. The team of Imperial College³ has tested extensively wall modeling to reduce the cost of LES applied to wall-bounded turbulence in a non-trivial geometry.

Most of the studies rely only on mean quantities such as the mean velocity profiles, friction or pressure distributions or turbulent intensities to judge the quality of the simulations. More in-depth analyses of the

flow, such as in Fröhlich *et al.*⁵ or in Breuer *et al.*,⁹ have however clearly shown that the flow is highly fluctuating at the considered Reynolds number. Quality of the prediction often depends on the value of the mean locations of the separation and reattachment points, which are highly unsteady and chaotic with strong irregular movements of the separation and reattachment lines. To analyse the quality of a simulation or a modeling assumption, it is thus necessary that the underlying dynamics is also correctly captured. Otherwise it is difficult to interpret possible discrepancies with the admitted reference values.

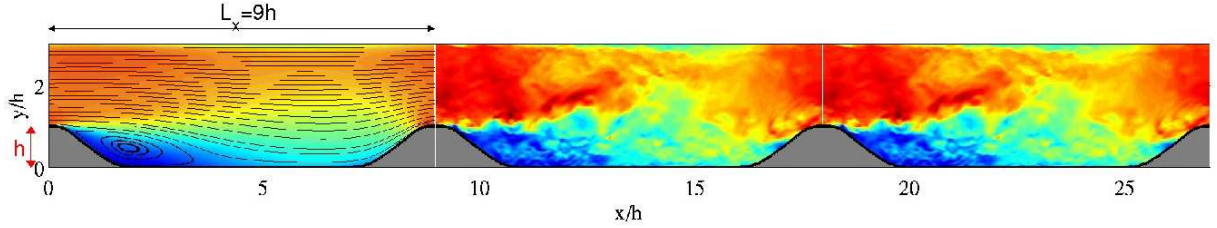


Figure 1. Periodic hill test case. The domain is replicated three times. The mean streamwise velocity and streamlines are shown in the first part and the instantaneous streamwise velocity at $Re=10595$ in the two others.

The aim of the present study is to improve our understanding of this complex dynamics which appears as a compendium of flow separation and reattachment from a curved boundary, generation of an unsteady shear layer surrounding the recirculation bubble, strong acceleration on the convex windward wall of the next hill, attached boundary layer on the ceiling subject to intense instantaneous pressure gradients, recycling of the turbulence due to the periodicity assumption. Previous studies have demonstrated that the boundary layer flow on the bottom wall is always far from equilibrium, which is very challenging for wall functions or RANS modeling of near-wall effects. The irregularity and intermittency of this moderate Reynolds-number flow is so important that it appears very cumbersome to identify reproducible coherent structures driving the flow dynamics. For that purpose, Breuer *et al.*⁹ have conducted a series of simulation by varying the Reynolds number from very low values. The shedding of vortices in the shear layer or the streamwise-elongated inclined structures are easily distinguishable at lower Reynolds numbers. The question of their representativeness for fully turbulent cases remains. Fröhlich *et al.*⁵ gathered and cross-compared a lot of statistical quantities including turbulent budgets and invariant maps to the mean profiles of velocity components and turbulent intensities to gain insight into the complex transfers leading to the peculiar features observed in this non-equilibrium turbulence. They notably investigated the 'splatting' effect when the barely reattached boundary layer encounters the windward wall of the next hill. Impingement of vortex clusters enhances the spanwise fluctuations and strong acceleration can lead to particular streamwise-oriented flow organisation, which certainly overwhelms the generation of Görtler-type instabilities related to the convex hill curvature. Their extensive analysis of the instantaneous dynamics also shed some light on the coherent structures which can hardly be identified in the separated shear layer. Small Kelvin-Helmholtz (KH) rolls are visible just ahead the separation line, even highly disrupted by the reentering turbulent spots. They never span the whole transverse extent due to the sinuous evolution of the separation line. The size of these pieces of coherent rolls grows very rapidly to form large scales, which further evolve toward inclined streamwise vortices, whose inclination is interestingly related to the principal axes of the average deformation tensor.

One unresolved issue which is addressed in the present work concerns the early birth of the shear layer and the rapid eruption of large scales, with a characteristic length-scale many times greater than the thickness of the initial shear. Sensitivity studies of numerical solutions to the computational grid have indeed shown that a refinement in the separation region can improve dramatically the results.³ The question is whether the physical phenomenon which is so important in this region is related to the separation process itself or to the early birth of the shear layer and the process leading rapidly to large vortices. The variability observed concerning the separation point is so strong that the second hypothesis can not be discarded. Another intriguing observation is that non monotonous convergence to the reference solution is sometimes noted such as in Xia *et al.*,¹² where the few formulated conjectures remain vague. A non monotonous convergence has also been observed in the present LES simulations at $Re=10595$ by refining the grid and was the starting point of the study.

The abstract is organised as follows: The numerical methods and the flow configuration are described in section II. A brief validation at a low Reynolds number is presented in section III and the results for the nominal case are discussed in section IV. Section V provides preliminary elements about the collective

interaction, which could play a role in the shedding of large scales. The last section gives a summary and the future directions.

II. Numerical setup

A. Governing equations

The governing equations are the compressible Navier-Stokes equations written for a curvilinear domain by using a coordinate transform. The physical space (x, y) is mapped into a Cartesian regular computational space (ξ, η) , and the third direction z is left unchanged. The set of equations for the unknown vector $\mathbf{U} = (\rho, \rho u, \rho v, \rho w, \rho E)^T$ writes:

$$\frac{\partial \mathbf{U}}{\partial t} + \frac{\partial \mathbf{F}_c}{\partial \xi} + \frac{\partial \mathbf{G}_c}{\partial \eta} + \frac{\partial \mathbf{H}}{\partial z} = 0 \quad (1)$$

by defining the curvilinear fluxes as:

$$\begin{cases} \mathbf{F}_c = \mathbf{F} \frac{\partial \xi}{\partial x} + \mathbf{G} \frac{\partial \xi}{\partial y} = \frac{1}{J} \left(\mathbf{F} \frac{\partial y}{\partial \eta} - \mathbf{G} \frac{\partial x}{\partial \eta} \right) \\ \mathbf{G}_c = \mathbf{F} \frac{\partial \eta}{\partial x} + \mathbf{G} \frac{\partial \eta}{\partial y} = \frac{1}{J} \left(-\mathbf{F} \frac{\partial y}{\partial \xi} + \mathbf{G} \frac{\partial x}{\partial \xi} \right) \end{cases} \quad (2)$$

where J is the Jacobian:

$$J = \begin{vmatrix} \frac{\partial x}{\partial \xi} & \frac{\partial y}{\partial \xi} \\ \frac{\partial x}{\partial \eta} & \frac{\partial y}{\partial \eta} \end{vmatrix} \quad (3)$$

$\mathbf{F} = \mathbf{F}_e - \mathbf{F}_v$, $\mathbf{G} = \mathbf{G}_e - \mathbf{G}_v$ and $\mathbf{H} = \mathbf{H}_e - \mathbf{H}_v$ are the sum of the inviscid (subscript **e**) and visco-thermal fluxes (subscript **v**) given by:

$$\begin{aligned} \mathbf{F}_e &= (\rho u, \rho u^2 + p, \rho uv, \rho uw, (\rho E + p)u)^T; & \mathbf{F}_v &= (0, \tau_{xx}, \tau_{xy}, \tau_{xz}, u\tau_{xx} + v\tau_{xy} + w\tau_{xz} - q_x)^T \\ \mathbf{G}_e &= (\rho v, \rho uv, \rho v^2 + p, \rho vw, (\rho E + p)v)^T; & \mathbf{G}_v &= (0, \tau_{xy}, \tau_{yy}, \tau_{yz}, u\tau_{xy} + v\tau_{yy} + w\tau_{yz} - q_y)^T \\ \mathbf{H}_e &= (\rho w, \rho uw, \rho vw, \rho w^2 + p, (\rho E + p)w)^T; & \mathbf{H}_v &= (0, \tau_{xz}, \tau_{yz}, \tau_{zz}, u\tau_{xz} + v\tau_{yz} + w\tau_{zz} - q_z)^T \end{aligned}$$

For an ideal gas, the specific total energy E is defined as:

$$E = p/[(\gamma - 1)\rho] + (u^2 + v^2 + w^2)/2, \quad \text{and} \quad p = \rho r T,$$

where T is the temperature, r the gas constant, and γ the ratio of specific heats. The viscous stress tensor τ_{ij} is modeled as a Newtonian fluid $\tau_{ij} = 2\mu S_{ij} - (2/3)\mu S_{kk}\delta_{ij}$, where $S_{ij} = (u_{i,j} + u_{j,i})/2$ is the rate of strain tensor and μ is the dynamic viscosity.

B. LES code

The convective terms are integrated in time using an explicit low-storage six-step Runge-Kutta scheme optimized in the wavenumber space.¹⁶ Because of their slower time evolution, the viscous terms are only integrated in the last substep. Optimized finite-differences on an eleven-point stencil¹⁶ are used for the derivatives of the convective fluxes, whereas standard fourth-order finite differences are used for the viscous and heat fluxes. At the last substep, a selective filtering on an eleven-point stencil¹⁶ is incorporated in each direction to eliminate grid-to-grid unresolved oscillations. It is applied with an amplitude of 0.2. On the wall boundary, the no-slip conditions $u = v = w = 0$ are imposed, with $\partial p / \partial n = 0$ for the Eulerian part, where n is the direction normal to the solid surface. The finite-difference stencil for the convective terms is progressively reduced down to the second order. At the wall, the temperature is calculated with the isothermal condition. The viscous stress terms are evaluated from the interior points by using fourth-order backward differences.

The LES strategy, combining a finite-difference scheme with good spectral properties with the use of a selective filtering without an additional eddy-viscosity model, bears some similarities with some new trends

of the LES approach. The explicit filtering provides a smooth defiltering by removing the fluctuations at wavenumbers greater than the finite-difference scheme resolvability. As demonstrated by Ref. 17, the effect of the Approximate Deconvolution Model (ADM) is globally similar to the convolution with an explicit filter. Moreover, the selective filtering induces a regularization similar to that used in the ADM procedure, even if the coefficient is taken constant. Since it does not affect the resolved scales, the exact value of the coefficient is not crucial¹⁸. Another advantage is the versatility of this LES strategy, since no additional effort is required, whereas more elaborate models can induce 20% to one order of additional cost.

C. Flow configuration

Figure 1 shows a sketch of the streamwise-periodic-hill channel flow configuration. The exact shape functions of the hill can be found in the ERCOFTAC website.¹³ The dimensions of the domain are $L_x=9h$; $L_y=3.035h$; $L_z=4.5h$, where h is the height of the hill. The fluid flows from left to right. In the simulation, the upper and lower boundaries are constituted by isothermal solid walls and no-slip velocity boundary conditions are used. Periodic boundary conditions are implemented in the streamwise x - and spanwise z -directions. Since the flow solver is compressible, we have fixed a relatively low value for the Mach number, $M=0.2$. Another tricky point is the forcing function. The strategy described by Benocci and Pinelli¹⁹ is followed to impose a constant mass flux.

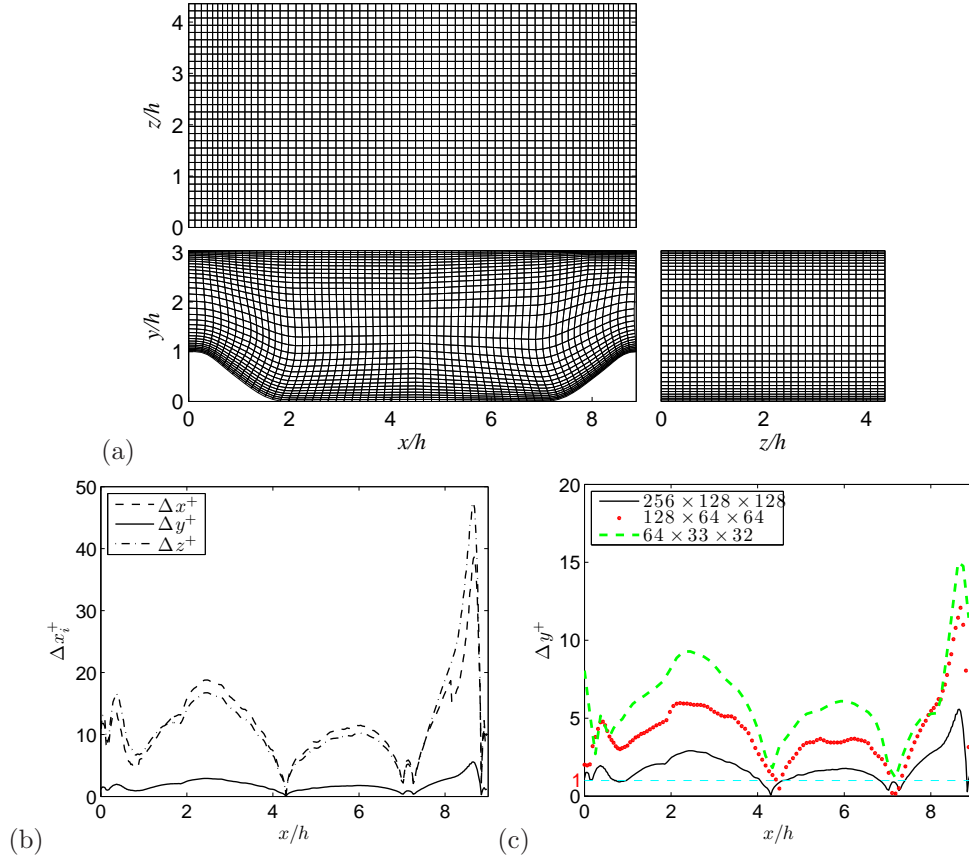


Figure 2. (a) View of the grid topology $64 \times 33 \times 32$; (b) resolution in wall coordinates Δx_i^+ for grid $256 \times 128 \times 128$ and (c) streamwise evolution of Δy^+ for the different grids where the horizontal dashed line denotes $\Delta y^+ = 1$.

Four levels of grid have been constructed by refining by a factor two in each direction from $64 \times 33 \times 32$ points to $512 \times 256 \times 256$ points. The coarsest one is represented in Fig. 2(a) for clarity reasons. The topology of the finer grids is identical. The resolution in terms of wall units, $\Delta x_i^+ = u_\tau \Delta x_i / \nu$, is provided in Fig. 2(b) and (c). The computational meshes are cut in blocks of 32^3 using MPI libraries. The $64 \times 33 \times 32$, $128 \times 64 \times 64$ and $256 \times 128 \times 128$ have run on 2, 16 and 128 cores, representing 1.3, 55.8 and 460.5 CPU days, respectively. Table 1 summarizes the different simulations that have been run, and which will be discussed in the final paper.

Case	Re	Grid	Nb flow-through (T_{avg})	$\Delta t U_b / h / 10^{-3}$
# 1	700	$64 \times 33 \times 32$	55.6 (500)	1.25
# 2	700	$128 \times 64 \times 64$	85.8 (772)	0.86
# 3	2800	$64 \times 33 \times 32$	27.7 (250)	1.25
# 4	2800	$128 \times 64 \times 64$	85.8 (772)	0.86
# 5	2800	$256 \times 128 \times 128$	30.1 (271)	0.34
# 6	5600	$64 \times 33 \times 32$	55.6 (500)	1.25
# 7	5600	$128 \times 64 \times 64$	85.8 (772)	0.86
# 8	5600	$256 \times 128 \times 128$	30.1 (271)	0.34
# 9	10595	$64 \times 33 \times 32$	55.6 (500)	1.25
# 10	10595	$128 \times 64 \times 64$	85.8 (772)	0.86
# 11	10595	$256 \times 128 \times 128$	30.1 (271)	0.34
# 12	19000	$256 \times 128 \times 128$	30.1 (271)	0.34
# 13	19000	$512 \times 256 \times 256$	30.1 (271)	0.15

Table 1. Simulated cases.

III. Code validation at Re=2800

To gain confidence in the particular numerical algorithm retained in the study, first results for the convergence of LES at a smaller Reynolds number, Re=2800, are presented.

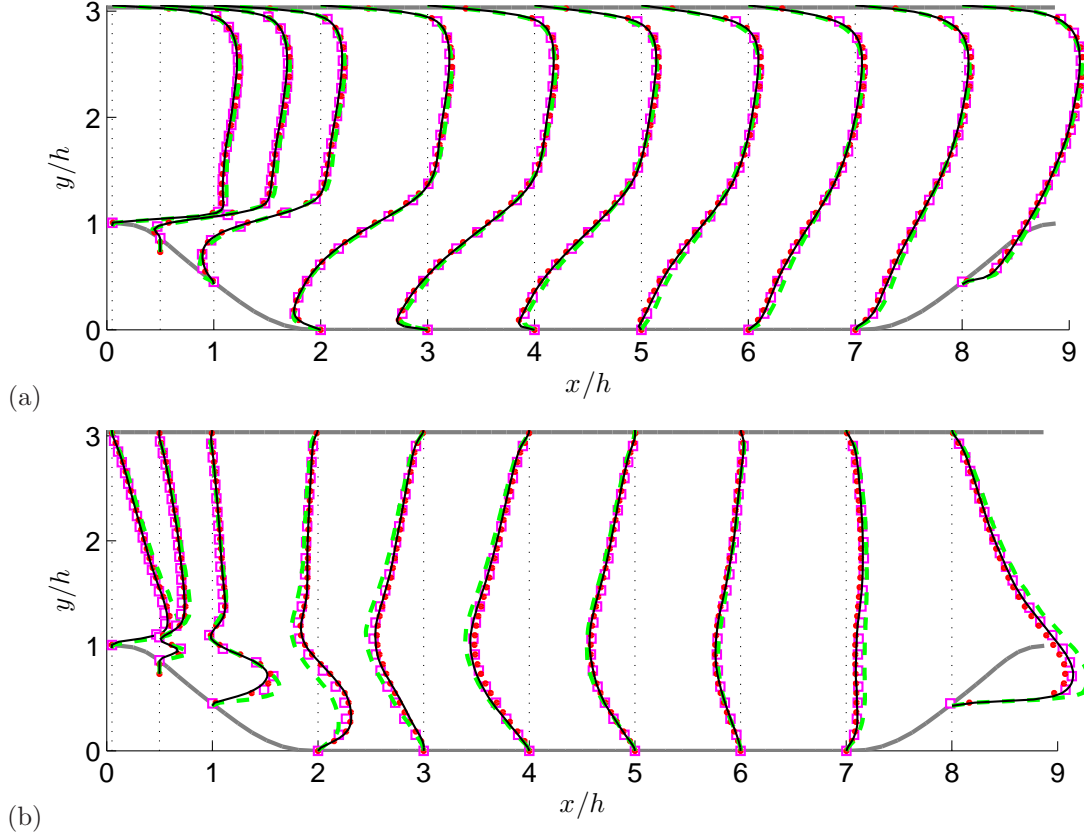


Figure 3. Grid convergence for the periodic hill at Re=2800: (—) $64 \times 33 \times 32$ (65000 pts); (••) $128 \times 64 \times 64$ (0.5 Mpts); (—) $256 \times 128 \times 128$ (4.2 Mpts); (□□) DNS Breuer *et al.*⁹ (code MGLET, 48 Mpts). (a) Mean streamwise velocity \bar{u} , (b) mean vertical velocity \bar{v} .

At this less-demanding Re, well established DNS can be used with confidence as reference. For instance, the differences between the DNS of Breuer *et al.*⁹ with MGLET code (second-order discretization based on immersed boundaries) with 231 million points and the DNS of Moxey, Sherwin and Peiró¹⁵ (spectral solver) with 20.9 million points are very small. Our LES results are compared with data from MGLET (made available on the web¹³). Mean velocity profiles \bar{u} and \bar{v} are depicted in Fig. 3. A very good match is noted for the finest grid using the $256 \times 128 \times 128$ grid, thus only 4.2 million points. Turbulent intensities profiles $\overline{u'u'}$, $\overline{v'v'}$ and $\overline{u'v'}$ are shown in Fig. 4. Here again a very good agreement is obtained with the DNS study when using the finest grid. It is our belief that the comparison at Re=2800 and the grid refinement study when taken together, indeed, provide confidence that the computer code used in the present investigation has the resolution and accuracy for an in-depth study of flow dynamics.

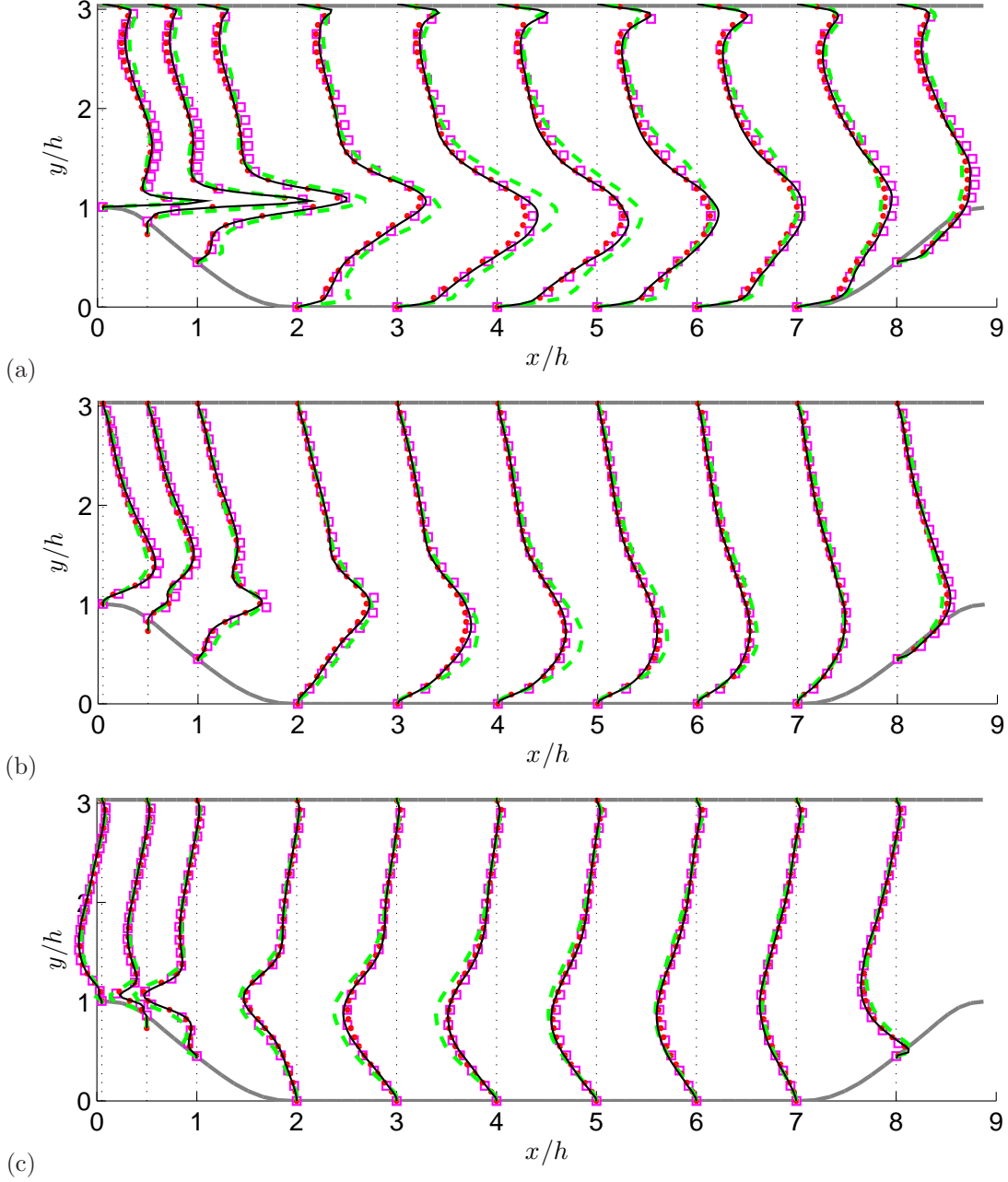


Figure 4. Grid convergence for the periodic hill at Re=2800: (— — —) $64 \times 33 \times 32$ (65000 pts); (●●●) $128 \times 64 \times 64$ (0.5 Mpts); (—) $256 \times 128 \times 128$ (4.2 Mpts); (□□□) DNS Breuer *et al.*⁹ (code MGLET, 48 Mpts). (a) Mean streamwise velocity u_{rms} , (b) mean vertical velocity v_{rms} and (c) turbulent intensity uv_{rms} .

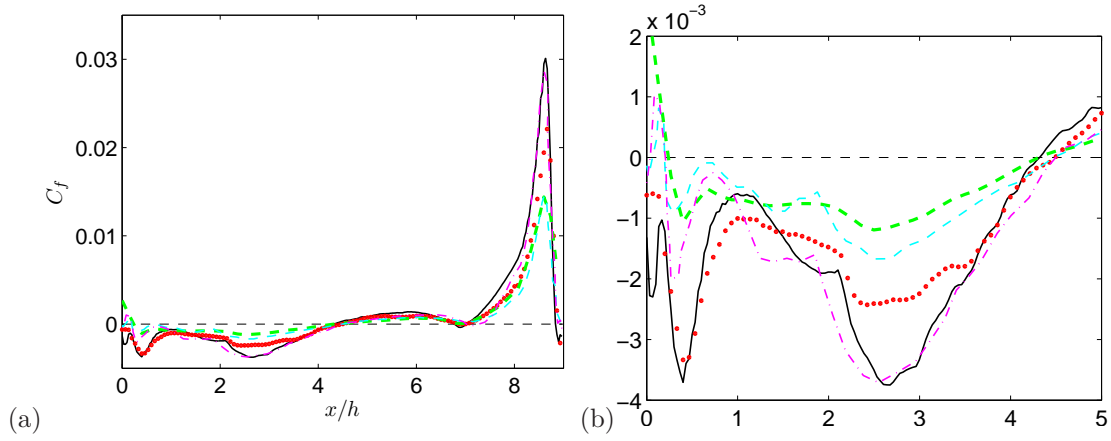


Figure 5. Periodic hill at $Re=10595$. (a) skin friction C_f ; (b) zoom (—) $64 \times 33 \times 32$ (65000 pts); (●●) $128 \times 64 \times 64$ (0.5 Mpts); (—) $256 \times 128 \times 128$ (4.2 Mpts); (—) LES Breuer *et al.* (13.1 Mpts); (—) LES Fröhlich *et al.* (4.6 Mpts).

IV. Grid convergence study at $Re=10595$

A global view of the mean and instantaneous streamwise velocity is given in Fig. 1, where the mean streamlines have been superimposed to the mean field. The flow separates at the hill crest and forms a large separation bubble. The distribution of the mean skin friction $C_f = 2\tau_w/(\rho U_b^2)$ along the bottom wall is depicted in Fig. 5 for the three grid resolutions and provides a first quantitative imprint of the mean flow topology. It is compared to the two reference LES of Breuer *et al.*⁹ and Fröhlich *et al.*⁵ A strong increase can be observed on the windward side and a maximum is reached just before the hill crest. The value of the maximum increases when the grid is refined. The value for the coarsest grid of $64 \times 33 \times 32$ is close to the one in the LES of Breuer *et al.*,⁹ whereas the value for the $256 \times 128 \times 128$ grid is closer to that obtained by Fröhlich *et al.*⁵ The Reynolds-number dependency of the peak value in Ref.⁹ indicates an increase with decreasing Re . The zoom of Fig. 5(b) focuses on the separation bubble. The minimum in the recirculation region near $x/h \simeq 2.5$ is more pronounced as the grid is refined. Here again the finest grid results are closer to the LES results of Fröhlich *et al.*,⁵ whereas the results for the coarsest grid follow the curve of Breuer *et al.*⁹ The latter have shown that the minimum is sharper when the Reynolds number rises. It can be concluded that the effective Reynolds number for the finest-grid LES or the simulation of Fröhlich *et al.*⁵ is lower than the one for the coarsest-grid LES or the simulation of Breuer *et al.*⁹ If the shape of C_f distribution are in good agreement between the different simulations, the behaviour of the mean separation point is different. The separation seems to occur just before the hill crest in our fine-grid LES, whereas it is located near $x/h \simeq 0.2$ in the two reference LES. Several oscillations of the shear stress are noticeable and correspond to the formation of small bubbles on the flat area of the top of the hill. We can conclude that the separation point is not clearly defined and can vary from one simulation to another without modifying significantly the reattachment point. This point is located near $x/h \simeq 4.5$ in the reference LES (or the medium-grid LES) whereas a value of $x/h \simeq 4.3$ is reached for the fine- and coarse-grid LES. It will be shown thanks to the mean velocity profiles that this value is in better agreement with the measurements of Breuer *et al.*⁹

Figures 6 and 7 show profiles for different streamwise stations for the mean velocity components and the turbulent intensities, respectively. The profiles are compared with the experimental points and the reference LES of Breuer *et al.*⁹ The agreement is reasonably good on the whole but some slight discrepancies can be observed. First the results closest to the measurements are provided by our fine-grid LES. It is notably visible for the profile of \bar{u} at $x/h = 5$ or 6 where the recovery of the bottom boundary layer is better captured. The levels of \bar{v} , which are one order of magnitude less, are also better reproduced (see $x/h = 3$ or 8 for instance). The biggest disparities are for the $\overline{u'u'}$ component. Here the levels are close to the reference LES and slightly underpredict the experimental levels. One striking point which can be identified on these plots is that the fine- and coarse-grid are close to the references whereas the results with the medium grid are farther. We can conclude that the grid convergence is not monotonous in our case, which has already been noted by other authors.¹² We will try in the following to propose conjectures which can explain this behaviour.

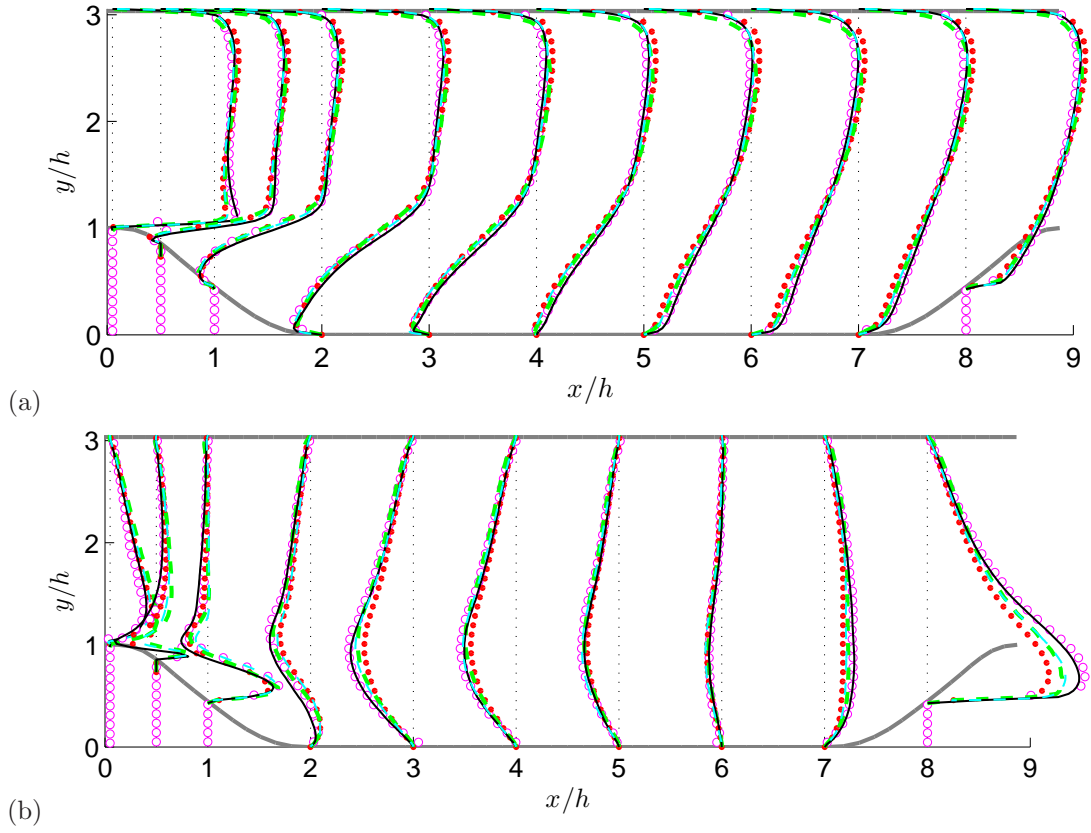


Figure 6. Grid convergence for the periodic hill at $Re=10595$: (—) $64 \times 33 \times 32$ (65000 pts); (\bullet) $128 \times 64 \times 64$ (0.5 Mpts); (—) $256 \times 128 \times 128$ (4.2 Mpts); (\circ) experiments Breuer *et al.*⁹ (—) LES Breuer *et al.*⁹ (code LESOCC, 31 Mpts). (a) Mean streamwise velocity \bar{u} , (b) mean vertical velocity \bar{v} .

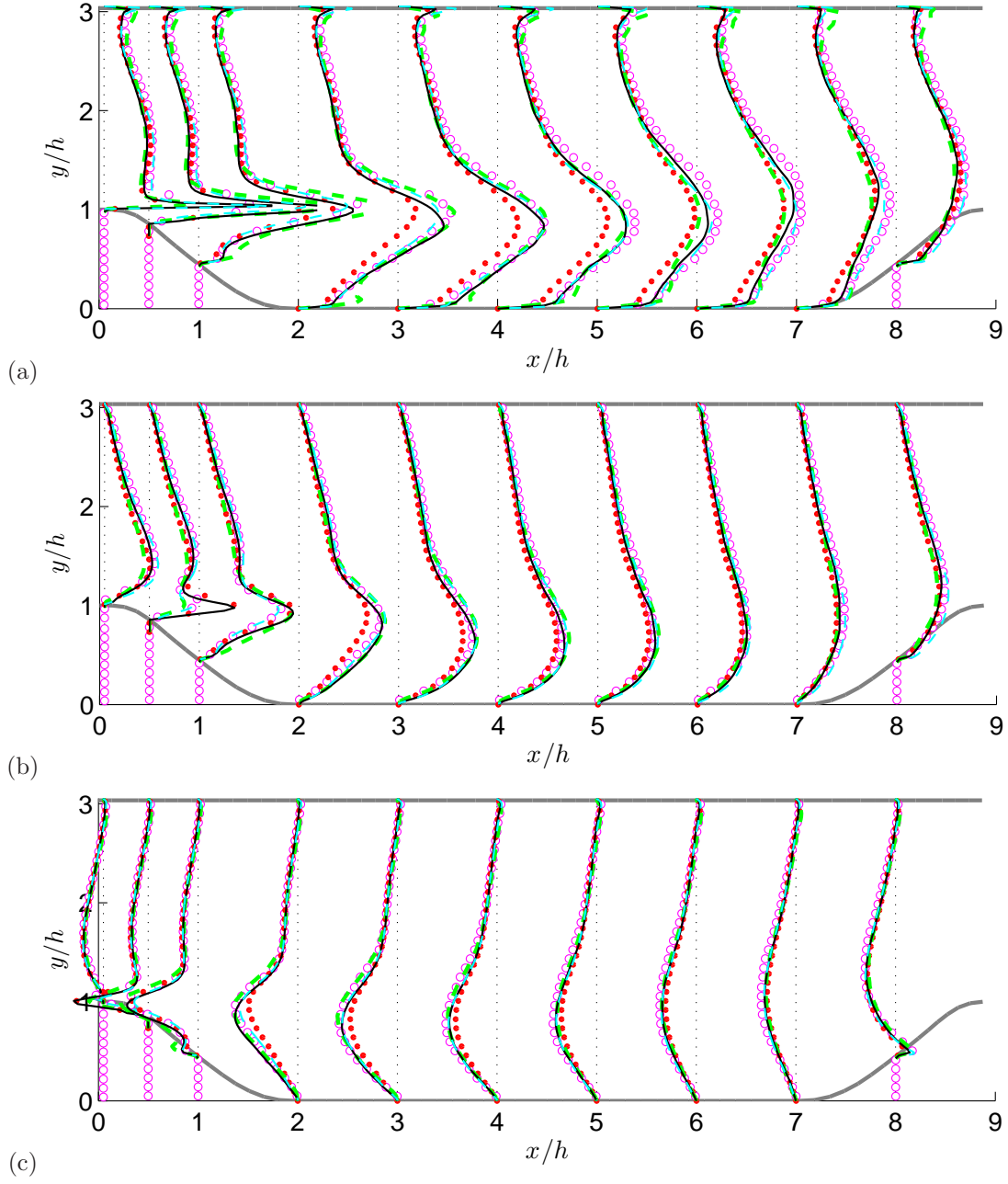


Figure 7. Grid convergence for the periodic hill at $Re=10595$: Mean flow: (—) $64 \times 33 \times 32$ (65000 pts); (●●) $128 \times 64 \times 64$ (0.5 Mpts); (—) $256 \times 128 \times 128$ (4.2 Mpts); (○) experiments Breuer *et al.*⁹ (—) LES Breuer *et al.*⁹ (code LESOCC, 31 Mpts). Turbulent intensit u_{rms} (a) v_{rms} (b) and uv_{rms} (c).

V. Analysis of shear layer dynamics

In order to explain the subtle discrepancies which are visible among the different simulations, a better understanding of the flow dynamics is desirable to identify the vortical structures that can drive the flow organization. Minima of the fluctuating pressure can be used to have a first view of the vortical structures. Instantaneous snapshots are given in Fig. 8. The first impression is that of a great variability in time. We pay a particular attention to the first part of the separated shear layer. The trace of small-size vortices is distinguishable in the first pictures and large scales emerge near $x/h \simeq 2$. This is reminiscent of the collective interaction phenomenon, which is scarcely studied in the literature. This badly known process is described in the next subsection. It is generally driven by a low-frequency component which force the large scales. Here the cavity between two hills is shallow, and can be categorized as closed,²⁰ and no feedback is noticeable.

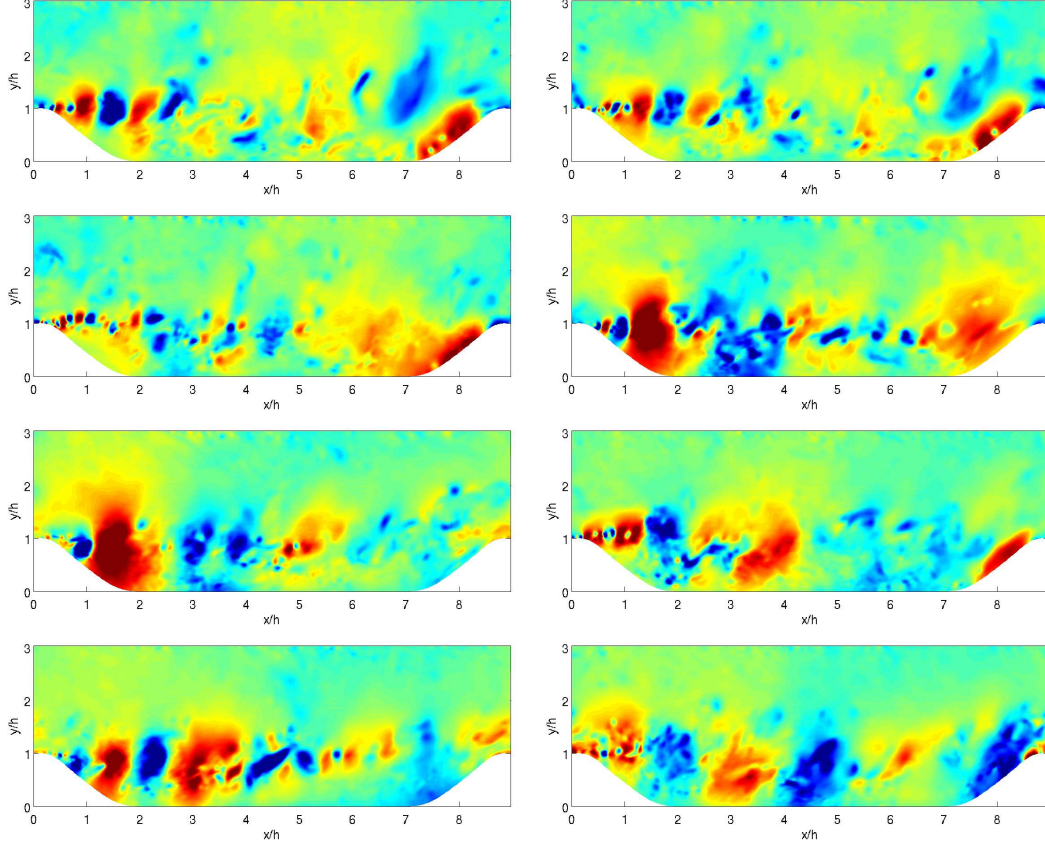


Figure 8. Periodic hill at $Re=10595$. Instantaneous snapshots of the fluctuating pressure.

A. Collective interaction phenomenon

The first description of a collective interaction has been done for mixing layers excited at a very low frequency.²¹ Figure 9(a) shows a mixing layer excited at a low frequency $f_0/8$, where the natural frequency f_0 is that of the most unstable Kelvin-Helmholtz (KH) instability. The sudden formation of a large-scale vortex arises from the fusion of a number of smaller vortices shedded at the natural frequency of the shear-layer. This phenomenon has been reproduced with our numerical solver on a grid of $900 \times 240 \times 100$ by exciting a plane mixing layer at f_0 and $f_0/8$, as illustrated in figure 9(b).

In experiments with a strong feedback and if the Reynolds number is sufficiently high, the feedback frequency represents a low-frequency frequency relative to the natural frequency scaled on the initial shear. A collective interaction can then drive the selection of the large structures entering in the feedback-loop process. This has been observed experimentally by Ho and Nosseir for an impinging jet²² or in numerical simulations of rectangular²³ or cylindrical²⁴ cavity flows. The instantaneous pressure field for a rectangular

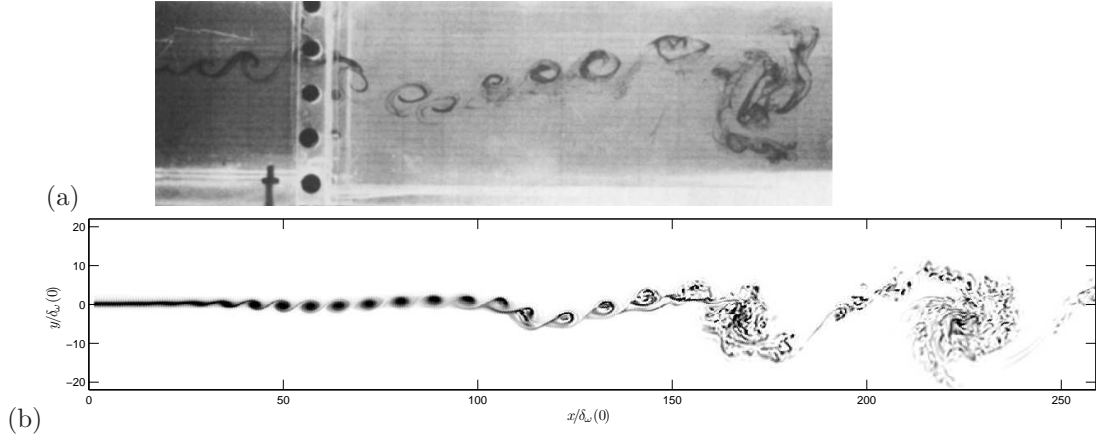


Figure 9. Collective interaction phenomenon: (a) Experiment of Ho and Huang²¹ for a mixing layer excited at a low frequency $f_0/8$, where f_0 is the fundamental KH frequency; (b) 3D simulation of a mixing layer excited at f_0 (with level $\alpha=5.10^{-4}$) and $f_0/8$ ($\alpha=30.10^{-4}$). The simulation is performed with the same solver on a grid of $900 \times 240 \times 100$.

cavity²³ with a length-to-depth ratio $L/D = 2$, a freestream Mach number $M=0.4$, and a Reynolds number $Re_L = 1.52 \times 10^6$ is depicted in Fig. 10(a). A closer look at the early shear-layer growth reveals that the size of the dominant structures is not related to the Kelvin-Helmholtz instability of the separated boundary layer, but is rather the results of the fusion of numerous Kelvin-Helmholtz vortices through a collective interaction after the separation corner. A sketch of the multiple fusion mechanism taken from Ho and Nosseir²² is reproduced in Fig. 10(b).

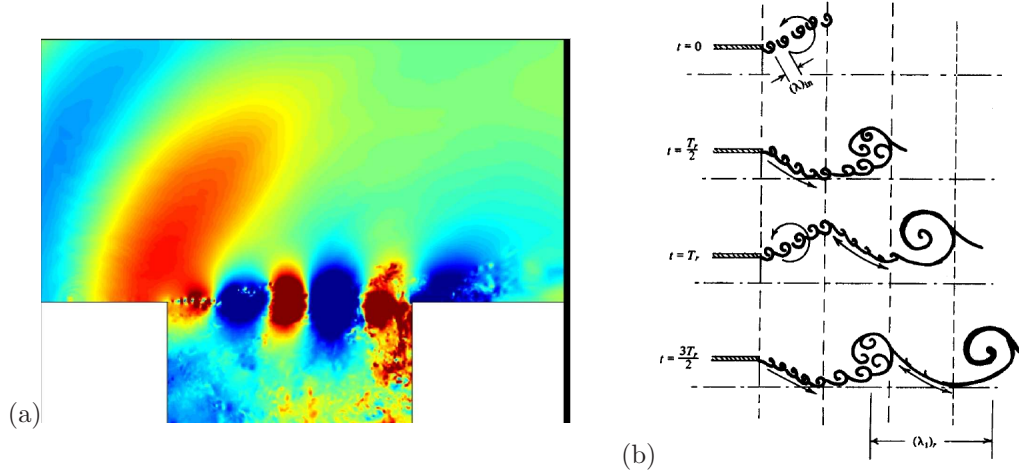


Figure 10. Collective interaction phenomenon: (a) Fusion of a number of smaller vortices near the upstream edge: fluctuating pressure field from a LES simulation of a rectangular cavity²³ (b) Sketch of the fusion mechanism, from Ho and Nosseir²² (note that the low-speed stream is now in the upper part).

B. Early growth of the mixing layer

The first task is to check the occurrence of Kelvin-Helmholtz instabilities in the upstream part of the shear layer shed at the separation point located somewhere on the hill crest. For that purpose, the mean streamwise velocity field \bar{u} is used to characterize the early growth of the mixing layer just after the hill restriction at $Re=10595$. Figure 11 shows close-up views for the different grid levels. The grid lines show that only few points are available to describe the thin shear after the separation. Profiles at successive streamwise locations are extracted by interpolating the velocity field on vertical lines. Then the centerline of the mixing layer is determined by searching loci $y_{0.5}$ where $\bar{u}=0.5U_\infty$, where U_∞ is the exterior velocity. These loci are marked

with black bullets in Fig.11.

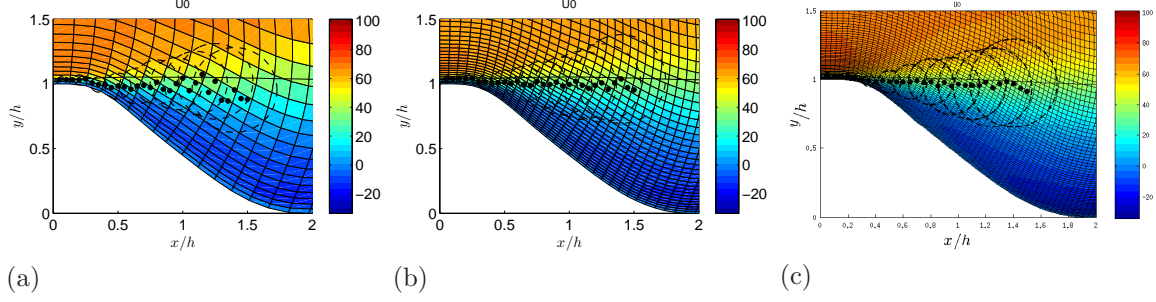


Figure 11. Periodic hill at $Re=10595$. Close-up views of the mixing layer growth for the different grid levels: (a) $64 \times 33 \times 32$; (b) $128 \times 64 \times 64$; (c) $256 \times 128 \times 128$. The colormap represents the mean streamwise velocity with the grid depicted; the black solid line is an iso-velocity $\bar{u}=40$ m/s; the black bullets represent the centroids of the mixing layer.

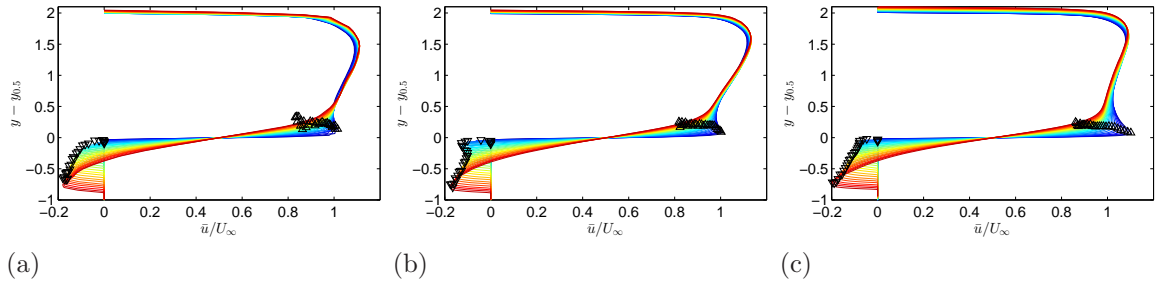


Figure 12. Periodic hill at $Re=10595$. Vertical extractions of mean streamwise velocity profiles plotted on the reduced coordinate $y - y_{0.5}$, where $y_{0.5}$ is the location of the inflection point for the different grid levels: (a) $64 \times 33 \times 32$; (b) $128 \times 64 \times 64$; (c) $256 \times 128 \times 128$. The streamwise locations are from $x/h=0.05$ to $x/h=1.5$ every 0.05 (from blue to red). For each profile, the upward and downward black triangles respectively denote the upper and lower bounds, y_{up} and y_{low} , for the integration of the momentum thickness, Eq.(4).

The \bar{u} -profiles are plotted as a function of the reduced coordinate $y - y_{0.5}$ in Fig.12 for the three grid levels. In order to examine the growth of the shear layer after separation from the hill crest, Fig.13(a) shows the evolution of the momentum thickness defined as :

$$\delta_\theta = \int_{y_{low}}^{y_{up}} \frac{\bar{u}}{U_\infty} \left(1 - \frac{\bar{u}}{U_\infty} \right) dy \quad (4)$$

where the integration bounds y_{up} and y_{low} are defined in Fig.12. The vorticity thickness defined as:

$$\delta_\omega = \frac{U_\infty}{\left(\frac{\partial \bar{u}}{\partial y} \right)_{\max}} \quad (5)$$

is plotted Fig.13(b). The momentum thickness growth is linear by parts and three regions can be distinguished: the first between $x/h = 0$ and 0.3 with a growing rate $d\delta_\theta/dx \simeq 0.032$ (cyan dash-dotted line), the second between $x/h = 0.3$ and 0.8 with $d\delta_\theta/dx \simeq 0.06$ (blue dash-dotted line). The third region extends after $x_1/L = 0.8$. The shear layer stops to grow and its thickness then decreases and oscillates. Some discrepancies can be noted between the three grid resolutions. The initial momentum thickness is greater as the grid is coarser and the saturation appears earlier with the $64 \times 33 \times 32$ -grid. The initial velocity gradient is more diffuse due to the number of points used to describe it.

The initial growth rate is close to the value of 0.035 observed for turbulent mixing layer.²⁵ Since the channel center is fulfilled by turbulent structures turning into the computational box, the shear layer experiences a highly turbulent environment and therefore spreads as a free turbulent mixing layer. After this initial phase, the growth rate is still higher. High values of $d\delta_\theta/dx \simeq 0.06$ have been previously noted for a

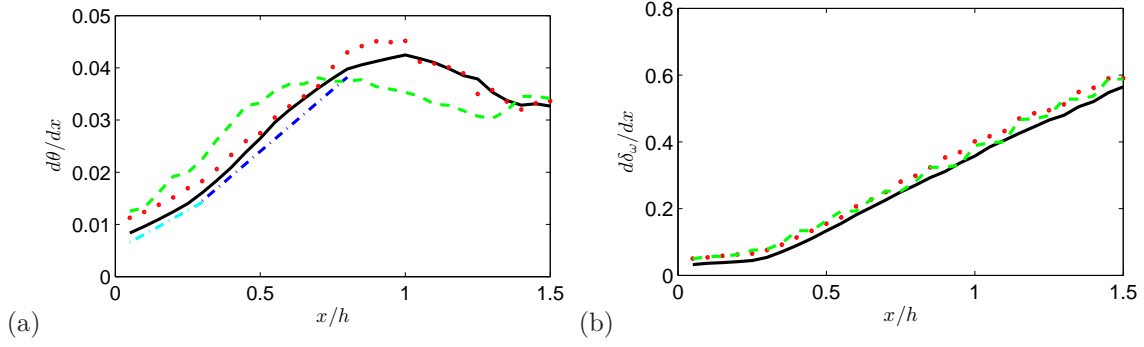


Figure 13. Periodic hill at $Re=10595$. Mixing layer growth through (a) momentum thickness; (b) vorticity thickness: (—■—) $64 \times 33 \times 32$ (65000 pts); (●●) $128 \times 64 \times 64$ (0.5 Mpts); (—) $256 \times 128 \times 128$ (4.2 Mpts).

forced mixing layer²⁵ or high-Reynolds-number cavity flows.²⁶ It is believed that this is the indication of a collective interaction to reach large-scale rolls in the mixing layer.

The analysis of the vorticity thickness leads to slightly different conclusions where the three grid levels exhibit roughly the same behaviour with a quasi-linear growth rate after $x/h = 0.3$. The initial stage between $x/h = 0$ and 0.3 is marked by a lower growth rate as already observed for the momentum thickness. This first region should correspond to the formation of Kelvin-Helmholtz vortices at the natural frequency of the shear layer. This natural frequency can be determined by looking at the most unstable frequency of the shear layer given by the linear theory of stability of parallel flows. Following Michalke,²⁷ the frequency is $f \simeq 0.82U_\infty/\delta_\omega$. Figure 14 displays the early development of the shear layer in this region. By dividing the reduced coordinate by the momentum thickness, a self-similar behaviour is indeed observed in this region in Fig.14(a). The wavelengths corresponding to Michalke's frequency are depicted with dashed circles in Fig.14(b), by using $\lambda = U_c/f$ and roughly $U_c = 0.5U_\infty$. Even on the finest grid of $256 \times 128 \times 128$, less than two points per wavelength are noticed, so that these K-H rolls can not be resolved in the present simulations. In the next subsection, velocity spectra are obtained to check if a preferred frequency is detectable.

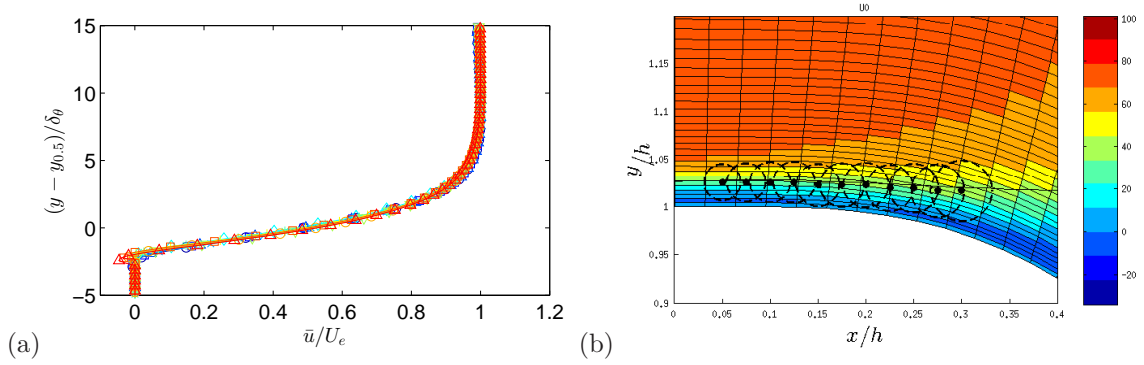


Figure 14. Periodic hill at $Re=10595$. Self-similarity of the streamwise velocity profiles in the early mixing layer (a). The profiles (from blue to red) are extracted at the locations marked by black bullets in the close-up view of the $256 \times 128 \times 128$ -grid (b).

C. Velocity spectra

The first velocity spectra which are depicted in Fig. 15 are located inside the fully developed flow. The two locations in the shear layer and in the recirculation zone are chosen to match those provided in the study by Fröhlich *et al.*⁵ First of all, these spectra for the three components of velocity do not show any indication of tonal humps. On the contrary, they are characteristic of established turbulence with a well-defined $-5/3$ decay law over more than a decade. This is representative of an inertial subrange, which is indicative that the flow behaves locally like isotropic turbulence. For high frequencies, a rapid decay is observed for the three velocity components and bears similarities with the spectra at the same locations reported in Fröhlich *et al.*⁵ The fall-off is directly driven by the spatial resolution, so it is related to the LES

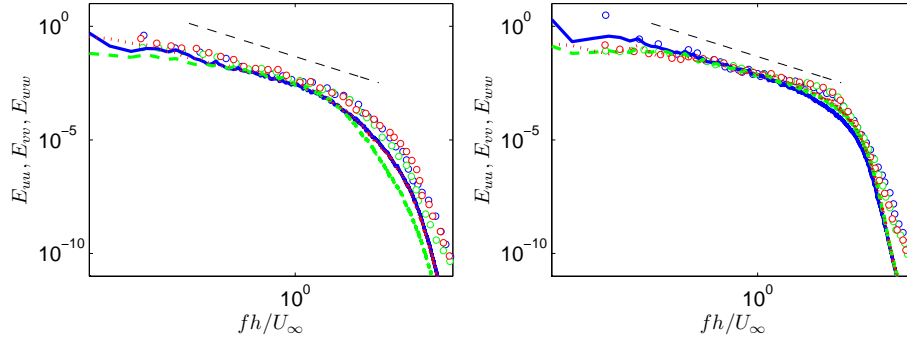


Figure 15. Periodic hill at $Re=10595$. Velocity spectra in the center of the recirculation zone $(x/h, y/h)=(2.15, 0.49)$ (a) and in the center of the shear layer $(x/h, y/h)=(2.23, 1.13)$ (b). Comparisons of the fine-grid $256 \times 128 \times 128$ LES (lines) and LES of Fröhlich *et al.*⁵ (symbols): E_{uu} — / \circ ; E_{vv} — — / \circ ; E_{ww} / \circ . The dashed black line has a slope of $f^{-5/3}$.

cut-off wavenumber. The spectral levels are not decaying at very low frequency and, as shown by Fröhlich *et al.*,⁵ low-frequency modulations are linked to the return time of the periodic flow. So the characteristic length of the low-frequency content is L_x .

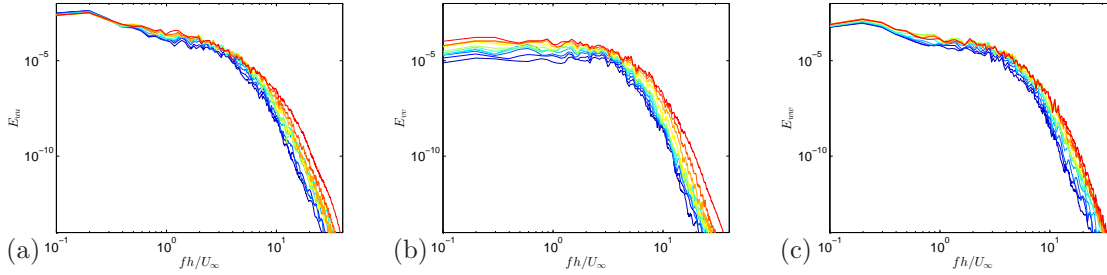


Figure 16. Periodic hill at $Re=10595$. Velocity spectra on the centerline of the mixing layer for longitudinal (a), vertical (b) and spanwise (c) components of velocity. Locations x/h of spectra (blue to red) are 0; 0.03; 0.06; 0.10; 0.13; 0.16; 0.19; 0.23; 0.26; 0.29; 0.33.

Next two series of spectra at successive streamwise locations are depicted for the first region of reduced shear-layer spreading and for the second region with a large growth rate in Fig.16 and 17 respectively. In the first region, where the shedding of natural K-H instabilities is expected, an enrichment of the spectra can be noticed, e.g. for the vertical component in Fig.16(b). But no trace of tonal component is visible. In the region of intense growth, the spectral content is seen to be almost identical in Fig.17 for the three velocity components, and is rather characteristic of a fully turbulent flow. We can conclude that there are no preferred size of the coherent structures which are observed on instantaneous snapshots, such as in Fig. 8. The great variability in time makes hard to identify the collective interaction process. The cavity between the hills can be categorized as closed, with flow reattachment on the floor. Consequently, no feedback loop is able to fix the size of the large-scales.

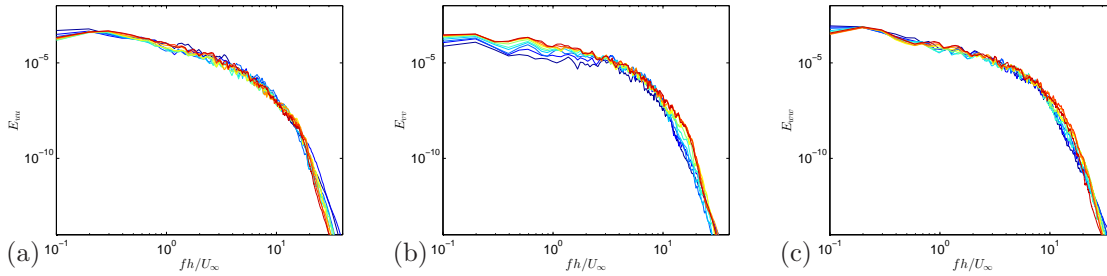


Figure 17. Periodic hill at $Re=10595$. Velocity spectra on the centerline of the mixing layer for longitudinal (a), vertical (b) and spanwise (c) components of velocity. Locations x/h of spectra (blue to red) are 0; 0.06; 0.13; 0.21; 0.28; 0.36; 0.44; 0.51; 0.58; 0.66.

VI. Conclusions and future work

High-accuracy large-eddy simulations of the flow in a channel with streamwise-periodic constrictions have been conducted and show an overall good agreement with the references for this well-documented benchmark case. Better agreement with the experiments than the published LES is obtained with a reduced number of grid points thanks to the use of high-order algorithms minimizing dissipation and dispersion errors. A striking point is that the grid convergence study is not monotonous for $Re=10595$. Details of the flow dynamics are investigated to explain this behaviour. The principal conjecture is that the resolution near the early birth of the separated shear layer plays a significant role. The mechanism leading to large vortices in the shear layer indeed bears similarities with the collective interaction phenomenon, which has been encountered for mixing layer excited by a low-frequency component. Further work is required to characterize this complex process highly disrupted by the turbulent fluctuations turning into the periodic box. A high spreading rate of the mixing layer has been observed but spectral analysis is not able to shed new light on this complex phenomenon since no preferred frequency is noticeable for this particular flow. Lagrangian tracking of pressure minima in the early shear layer or stochastic estimation will be used in future work to reduce the behaviour of coherent structures.

Besides, the collective interaction phenomenon should be more intense for higher Reynolds number since the scale gap between the thickness of the initial shear and the size of the box is increased. That is why new simulations at a $Re_h = 19000$ have been realized on a grid of $512 \times 256 \times 256$ points (Fig. 18). They compare favorably to the experiments at the same value of the Reynolds number available in the database.¹³ At this higher Reynolds number, the scale separation between the structures scaling on the initial shear and the large-scale motions is reinforced.

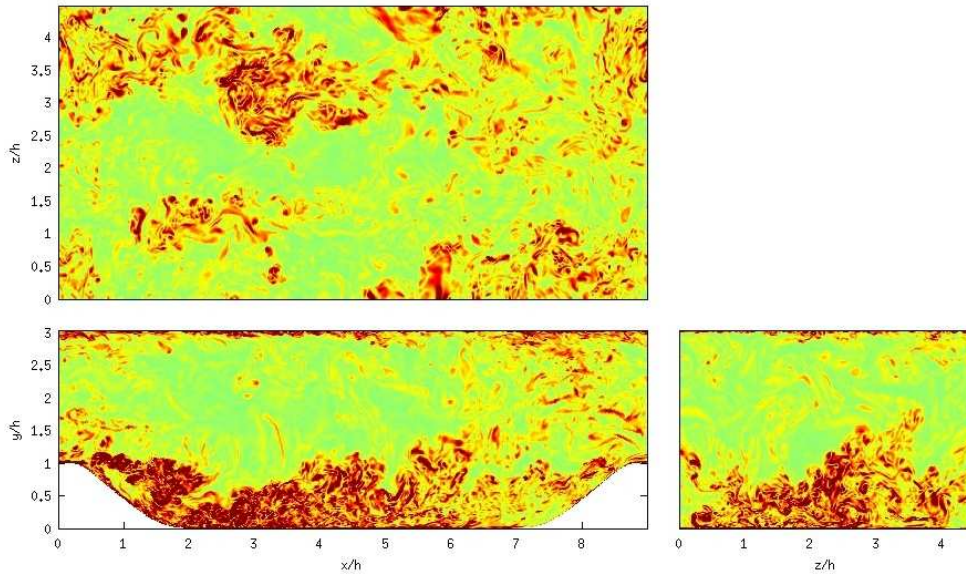


Figure 18. Periodic hill at $Re=19000$. Instantaneous snapshots of the vorticity norm $||\omega||$ for a grid of $512 \times 256 \times 256$. Clusters of small scales are visible.

References

- ¹Mellen, C., Fröhlich, J., and Rodi, W., “Large eddy simulation of the flow over periodic hills,” *Proc. IMACS World Congress*, edited by M. D. . R. Owens, Lausanne, 2000.
- ²Davidson, L. and Peng, S., “Hybrid LES-RANS modelling: a one-equation SGS model combined with a $k-\omega$ model for predicting recirculating flows,” *Int. J. Numer. Meth. Fluids*, Vol. 43, 2003, pp. 1003–1018.
- ³Temmerman, L., Leschziner, M., Mellen, C., and Fröhlich, J., “Investigation of wall-function approximations and subgrid-scale models in large-eddy simulation of separated flow in a channel with streamwise periodic constrictions,” *International Journal of Heat and Fluid Flow*, Vol. 24, 2003, pp. 157–180.
- ⁴Temmerman, L., Hadziabdić, M., Leschziner, M., and Hanjalic, K., “A hybrid two-layer URANS-LES approach for large eddy simulation at high Reynolds numbers,” *International Journal of Heat and Fluid Flow*, Vol. 26, 2005, pp. 173–190.

- ⁵Fröhlich, J., Mellen, C., Rodi, W., Temmerman, L., and Leschziner, M., "Highly resolved large-eddy simulation of separated flow in a channel with streamwise periodic constrictions," *J. Fluid Mech.*, Vol. 526, 2005, pp. 19–66.
- ⁶Tessicini, F., Temmerman, L., and Leschziner, M., "Approximate near-wall treatments based on zonal and hybrid RANS-LES methods for LES at high Reynolds numbers," *International Journal of Heat and Fluid Flow*, Vol. 27, 2006, pp. 789–799.
- ⁷Fröhlich, J. and von Terzi, D., "Hybrid LES-RANS methods for the simulation of turbulent flows," *Progress in Aerospace Sciences*, Vol. 44, 2008, pp. 349–377.
- ⁸Zieffe, J., Stolz, S., and Kleiser, L., "Large-eddy simulation of separated flow in a channel with streamwise-periodic constrictions," *AIAA Journal*, Vol. 46, 2008, pp. 1705–1718.
- ⁹Breuer, M., Peller, N., Rapp, C., and Manhart, M., "Flow over periodic hills - Numerical and experimental study in a wide range of Reynolds numbers," *Computers and Fluids*, Vol. 38, 2009, pp. 433–457.
- ¹⁰Duprat, C., Balarac, G., Métais, O., Congedo, P., and Brugière, O., "A wall-layer model for large-eddy simulations of turbulent flows with/out pressure gradient," *Phys. Fluids*, Vol. 23, 2011, pp. 015101.
- ¹¹Balakumar, P., Rubinstein, R., and Rumsey, C., "DNS, enstrophy balance, and the dissipation equation in a separated turbulent channel flow," *43rd AIAA Fluid Dynamics Conference*, 24–27 June, San Diego, California, AIAA Paper 2013-2723, 2013.
- ¹²Xia, Z., Shi, Y., Hong, R., Xiao, Z., and Chen, S., "Constrained large-eddy simulation of separated flow in a channel with streamwise-periodic constrictions," *J. Turbulence*, Vol. 14, No. 1, 2013, pp. 1–21.
- ¹³Rapp, C., Breuer, M., Manhart, M., and Peller, N., "2D Periodic Hill Flow," ERCOFTAC QNET-CFD, http://qnet-ercoftac.cfms.org.uk/w/index.php/UFR_3-30
- ¹⁴Haase, W., Braza, M., and Revell, A., editors, *DESider - A European Effort on Hybrid RANS-LES Modelling; Results of the European-Union Funded Project, 2004-2007*, Vol. 103 of *Notes on Numerical Fluid Mechanics and Multidisciplinary Design*, Springer, 2009.
- ¹⁵Kroll, N., Hirsch, C., Bassi, F., Johnston, C., and Hillewaert, K., editors, *IDIHOM: Industrialization of High-Order Methods - A Top-Down Approach; Results of a Collaborative Research Project Funded by the European Union, 2010-2014*, Vol. 128 of *Notes on Numerical Fluid Mechanics and Multidisciplinary Design*, Springer, 2015.
- ¹⁶Bogey, C. and Bailly, C., "A family of low dispersive and low dissipative explicit schemes for noise computation," *J. Comput. Phys.*, Vol. 194, 2004, pp. 194–214.
- ¹⁷Mathew, J., Lechner, R., Foysi, H., Sesterhenn, J., and Friedrich, R., "An explicit filtering method for large eddy simulation of compressible flows," *Phys. Fluids*, Vol. 15, No. 8, 2003, pp. 2279–2289.
- ¹⁸Bogey, C. and Bailly, C., "Large eddy simulations of round jets using explicit filtering with/without dynamic Smagorinsky model," *International Journal of Heat and Fluid Flow*, Vol. 27, 2006, pp. 603–610.
- ¹⁹Benocci, C. and Pinelli, A., "The role of the forcing-term in large-eddy simulation of equilibrium channel flow," *Engineering turbulence modeling and experiments*, edited by W. R. . E. Ganic, 1990, pp. 287–296.
- ²⁰Gloerfelt, X., "Cavity noise," *Aerodynamic noise from wall-bounded flows*, VKI Lectures, March 9–13 2009.
- ²¹Ho, C.-M. and Huang, L.-S., "Subharmonics and vortex merging in mixing layers," *J. Fluid Mech.*, Vol. 119, 1982, pp. 443–473.
- ²²Ho, C.-M. and Nossier, N., "Dynamics of an impinging jet. Part 1. The feedback phenomenon," *J. Fluid Mech.*, Vol. 105, 1981, pp. 119–142.
- ²³Gloerfelt, X., "Large Eddy Simulations of high Reynolds number cavity flows," *Workshop Direct and Large-Eddy Simulation 8*, July 7–9, Eindhoven, The Netherlands, 2010.
- ²⁴Chicheportiche, J. and Gloerfelt, X., "Effect of a turbulent incoming boundary layer radiation by the flow over cylindrical cavities," *17th AIAA/CEAS AeroAcoustics Conference*, 6–8 June, Portland, Oregon, AIAA Paper 2011-2588, 2011.
- ²⁵Oster, D. and Wygnanski, I., "The forced mixing layer between parallel streams," *J. Fluid Mech.*, Vol. 123, 1982, pp. 91–130.
- ²⁶Gloerfelt, X., Bogey, C., and Bailly, C., "Numerical evidence of mode switching in the flow-induced oscillations by a cavity," *Int. J. of Aeroacoustics*, Vol. 2, No. 2, 2003, pp. 99–124.
- ²⁷Michalke, A., "On the inviscid instability of the hyperbolic-tangent velocity profile," *J. Fluid Mech.*, Vol. 19, 1964, pp. 543–556.